Scripta Materialia 192 (2021) 115–119

Contents lists available at ScienceDirect

Scripta Materialia

journal homepage: www.elsevier.com/locate/scriptamat

Grain boundary character distribution in an additively manufactured austenitic stainless steel

Majid Laleh[a,b], Anthony E. Hughes[b,c], Mike Y. Tan[a,b], Gregory S. Rohrer[d], Sophie Primig[e], Nima Haghdadi[e,*]

[a] School of Engineering, Deakin University, Waurn Ponds, VIC 3216, Australia
[b] Institute for Frontier Materials, Deakin University, Waurn Ponds, VIC 3216, Australia
[c] Commonwealth Scientific and Industrial Research Organisation (CSIRO), Mineral Resources, Private Bag 10, Clayton South, VIC 3169, Australia
[d] Department of Materials Science and Engineering, Carnegie Mellon University, Pittsburgh, PA 15213-3890, USA
[e] School of Materials Science & Engineering, UNSW Sydney, Sydney, NSW 2052, Australia

ARTICLE INFO

Article history:
Received 1 September 2020
Revised 7 October 2020
Accepted 9 October 2020

Keywords:
Grain boundary engineering
Additive manufacturing
Austenitic stainless steel

ABSTRACT

The grain boundary character distribution (GBCD) in an austenitic stainless steel produced by additive manufacturing (AM) in both as-built and annealed conditions was studied. Relatively fine grains and a non-fibre texture was achieved by AM, and as-built structure showed a high population of Σ3 boundaries. A five-parameter GBCD analysis revealed that the microstructure is mostly dominated by highly incoherent Σ3 boundaries. The grain boundary network also consisted of random high angle, coherent Σ3s terminating on (111) planes with a pure twist character, and tilt Σ9 boundaries. The findings show prospects for the possibility of engineering the grain boundary network of materials *in-situ*, via the stress and heat induced by the thermal cycles during AM.

Laser powder bed fusion (LPBF) is an additive manufacturing (AM) technology that uses a high-energy laser beam to melt powder particles to consolidate a metallic part [1,2]. Upon laser irradiation of a powder bed, a melt pool forms and then solidifies at a very fast rate (up to 10^7 K/s [3]). Individual tracks join together during succeeding laser passes to form a 3D part. During LPBF, the material experiences complex thermal gradients and gyrations which subsequently result in a unique microstructure. These unique microstructural features can lead to superior mechanical properties [4,5] and corrosion resistance [6–8] e.g. in LPBF austenitic stainless steels, exceeding those of their traditionally manufactured counterparts. A current focus in the metal AM research community is directed towards understanding such complex microstructures in order to develop metals and alloys with optimised properties of interest by altering processing variables [9].

Grain boundary engineering (GBE) has been the subject of intensive research during the last 40 years with the aim of introducing coincident site lattice (CSL) and low-angle grain boundaries (GBs) to mitigate undesirable intergranular phenomena such as corrosion, embrittlement and fracture [10–14]. While GBE has been studied for traditionally manufactured stainless steels, the potential of the thermomechanical hysteresis that a material experiences during AM for engineering microstructures is yet to be explored. Typical anisotropic microstructures reported in AM materials consisted of grains elongated towards the build direction with <100> and/or <110> texture [15,16]. Such morphology can be broken down via a change in laser scanning strategy, where a hierarchical microstructure can be formed that offers outstanding mechanical properties achieved either through microsegregation resulting from cellular solidification and/or via a network of dislocation-rich sub-boundaries [4,17]. It can be hypothesized that engineering the grain boundary network in austenitic stainless steel via AM may unlock additional unique properties in terms of corrosion, embrittlement and fracture resistance. This is because diffusivity, mobility, and segregation of a grain boundary are affected by its crystallography. However, an analysis of the formation mechanism and a detailed knowledge of the crystallographic character of CSL grain boundaries in AM microstructures is currently lacking. The current work reports on the possibility of *in-situ* GBE during AM of an austenitic stainless steel, and provides a full five-parameter macroscopic description of these boundaries. The results can be extended to several other face centred cubic (FCC) metals with low-to-medium stacking fault energy (SFE).

Argon-atomised 316L austenitic stainless steel (hereinafter 316L SS) powder with particle sizes between 5 and 45 μm was used. Cubes (10 × 10 × 10 mm^3) were produced using a LPBF machine

* Corresponding author.
E-mail address: nima.haghdadi@unsw.edu.au (N. Haghdadi).

https://doi.org/10.1016/j.scriptamat.2020.10.018
1359-6462/

(SLM Solutions, Group AG, Lübeck, Germany). A laser power of 150 W, scanning speed of 400 mm/s, hatch spacing of 80 µm and layer thickness of 30 µm were utilised. A meander hatching pattern with hatch angle of 67° was used. The processing was conducted under an argon atmosphere (O_2<100 ppm), and the base plate was pre-heated to 200°C. Printed samples covered most of the area of the baseplate. The presence of these samples was thought to retard the cooling rate thus contributing to the unusual microstructure observed in this study. Selected samples were annealed post-LPBF at 1000°C for 10 min followed by water quenching.

Samples were ground and polished following standard metallographic procedures down to 1 µm, and finished with 0.04 µm oxide polishing suspension. An electron backscatter diffraction (EBSD) detector in an FEG Quanta 3D FEI scanning electron microscope (SEM) at 20 kV, 8 nA and working distance of ~12 mm was used. Orientation data was recorded with a hexagonal grid with a 1 μm step size. The TSL-OIM software was used for acquisition and post processing of EBSD data. Three steps of data cleaning were implemented including (i) an iterative grain dilation routine with a 5 pixels grain size minimum, (ii) a single average orientation assignment with 5° tolerance angle, (iii) segmenting of curved GBs using a boundary deviation limit of 2 pixels.

Rotation angle/axis pairs (θ/<uvw>) were obtained from EBSD. The other two parameters for habit plane assignment, including the trace and inclination of the plane, were obtained using a stereological method, as described in [18]. This method requires the measurement of a large number of boundary segments (>50,000 for cubic structures [18]) to yield a statistically significant solution. In this work, >250,000 GB segments were collected for the as-printed and annealed samples. To mitigate the effects of anisotropic grain shapes and texture, orientation maps were obtained on three mutually perpendicular section planes. The GB plane distribution was measured in multiples of a random distribution (MRD), where an MRD higher than one means that a plane is observed more frequently than expected in a random distribution. Throughout the text, 'twist' and 'tilt' configurations refer to cases where the GB normal is parallel and perpendicular to the misorientation axis, respectively, and being 'symmetric' implies that boundaries have planes with identical indexes on both sides of a boundary [19].

Analysis of the as-built 316L SS microstructure in *XY, XZ* and *YZ* planes shows that grains are fine and elongated towards the build direction (*Z*) (Fig. 1a,b). Finer grains are visible at melt pool boundaries when viewed in *XZ* plane. This microstructure differs from the coarse columnar grains and sharp <100> or <110> texture parallel to the built direction observed in some previous reports for LPBF 316L SS [15,16,20]. Interestingly, annealing at 1000°C for 10 min did not significantly change the grain morphology and average grain size (Fig. 1c,d).

Mapping of CSL boundaries (using Brandon's criterion [21]) revealed that a large fraction of GBs (30.6%) in the as-built condition are Σ3 CSL boundaries with 60°/<111> misorientation. There was also a low fraction (~0.6%) of Σ9 CSL boundaries with 39°/<110> misorientation, mostly forming when two Σ3s intersect (Fig. 1b). The dominance of these boundaries was also revealed in the misorientation angle/axis distribution of the GBs showing a sharp peak at 60° with the corresponding axis vectors clustered around the <111> direction, and a secondary diffuse peak at 39° with corresponding axis vectors clustered around the <110> direction (Fig. 2a). Annealing changed neither the misorientation angle distribution of high angle GBs nor the fraction of Σ3 and Σ9 boundaries (30.4% and ~0.5%, respectively) (see Figs. 1d and 2b). The population of Σ9 boundaries was relatively low in as-built and annealed conditions compared to other FCC materials [22–25].

The extensive twinning observed in the LPBF sample is interesting and has not been reported for any LPBF-processed material, not even in alloys with high tendency for twinning such as copper. Such excessive twinning achieved by GBE usually takes place during annealing of a previously-deformed steel [10–13]. In the current study, LPBF has caused in-situ GBE, forming a GB network dominated by Σ3 boundaries, a microstructure that traditional GBE approaches only accomplished through mechanical deformation [11,13]. GBE in low-to-medium SFE FCC materials is traditionally carried out by repeated strain and annealing treatments. The corresponding microstructural evolution has been reported in between the regimes of grain growth, where there is no influence of stored strain energy, and recrystallisation, which is driven primarily by strain energy gradients [26]. Two commonly-used thermomechanical procedures to induce large Σ3 concentrations in these materials include: (i) a deformation up to 8% followed by annealing at temperatures below the recrystallisation temperature to supress nucleation of new grains but yet enabling reorientation of GBs towards low energy configurations (mainly Σ3 boundaries), and (ii) a multi-cycle straining up to 30% followed by short-time annealing at relatively high temperatures [26].

Usually, only a small amount of pre-strain is applied to induce a high concentration of twin (Σ3) boundaries during GBE, because a larger deformation energy triggers extensive dynamic recrystallisation (DRX) limiting twinning. Taking coarse-grained pure copper as a simple model for FCC alloys, Koo et al. [27] showed that deformations as low as 2% can reduce the incubation time for grain growth. Such low-level deformation causes a distortion of the GBs by extrinsic dislocations, activating rapid grain growth of selected GBs. However, our LPBF material did not experience any external deformation during processing. This implies that the non-uniform distributions of dislocations manifested as orientation gradients and residual stresses in LPBF parts provide the required driving force. A detailed understanding of the mechanisms of dislocation accumulation and strain gradients within LPBF steels is not yet established. However, it is speculated that the substantial energy frozen in the LPBF steel during rapid solidification as well as alternative compression and tensile loading during LPBF thermal cycles create strain within grains, usually manifested as misorientation gradients. This and the heat from melting of succeeding layers acts as driving force for Σ3 boundary formation. This can be observed in supplementary Fig. 1 where the topmost layer shows a significant lattice curvature. This is rational assuming that the top layer (the last-printed layer) is melted followed by rapid cooling. The extremely high cooling rate may partially freeze the solidified microstructure, avoiding the formation of Σ3s, while layers that were printed earlier experience multiple reheating processes which provides kinetic conditions for Σ3s formation and migration.

The absence of a GBE dominated microstructure in previous LPBF studies on the same stainless steel might be due to a difference in the extrinsic effects such as printing strategy and heat sink efficiency as well as intrinsic factors such as texture and grain size. The weak heat dissipation of printed samples provides the driving force for twins' migration. Moreover, the meander hatching pattern with hatch angle of 67° would contribute to texture randomization and break up of large elongated grains. Both <111> and <110> textures favour Σ3s as these boundaries can be described as a 60° or 70.5° around <111> and <110> axes, respectively [28,29]. This might be the main reason for the absence of Σ3 boundaries in previous studies that report a <100> texture [5,15,20,30]. The finer grain size observed in the current study might be another reason because there is a tendency for increased twinning with decreasing grain size [31].

Considering the significant role of the plane character on properties of GBs, the GB plane distribution was measured in the crystal reference frame for all GBs (Fig. 3). The distributions revealed an anisotropy with a maximum at the (111) position of ~1.22 and 1.35 MRD for the as-built and annealed conditions, respectively.

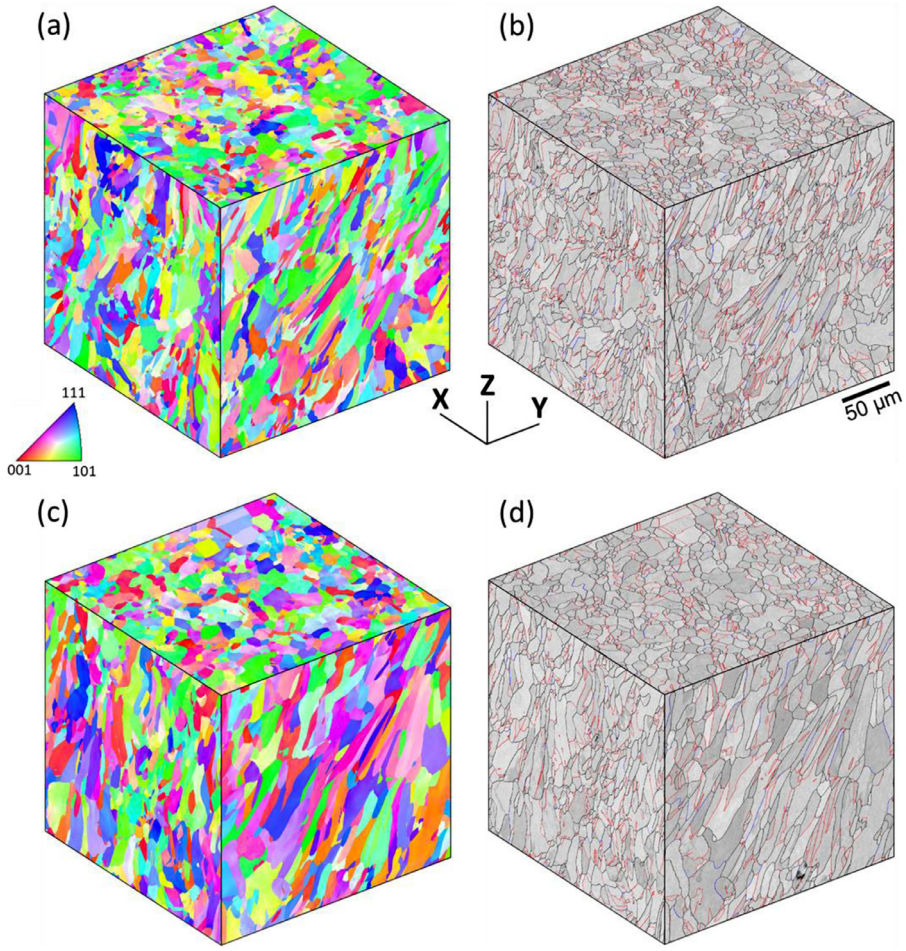

Fig. 1. (a,c) Inverse pole figure (IPF) map along the *Z* direction and (b,d) GB distribution maps (black, red and blue lines denote random, Σ3 and Σ9 boundaries, respectively) in (a,b) as-built and (c,d) annealed AM 316L SS at different cross sections. The two-dimensional *XY*, *XZ* and *YZ* sections are displayed as the surfaces of a cube to represent their relative orientations.

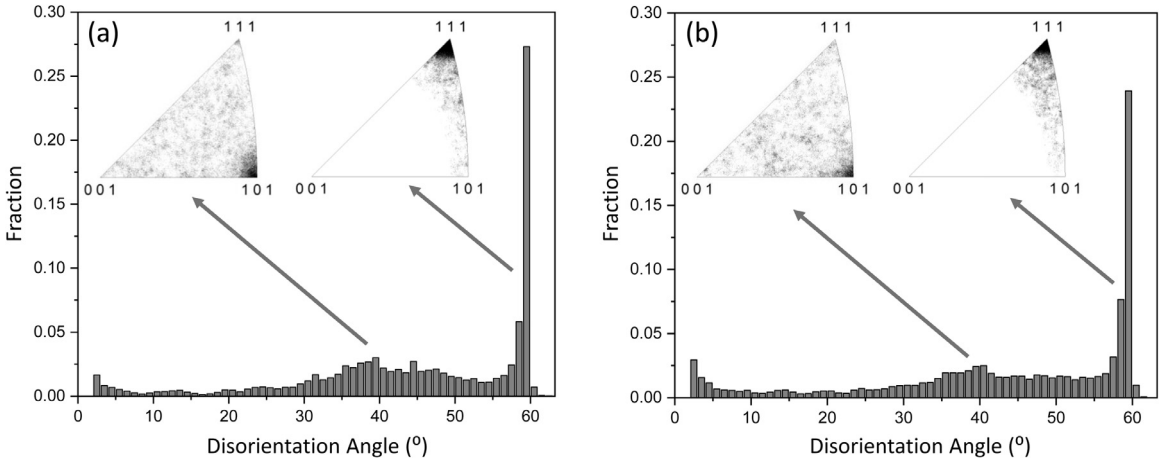

Fig. 2. GB misorientation angle/axis distribution in (a) as-built and (b) annealed AM 316L stainless steel.

This implies that the population of (111) planes was about 22% and 35% higher than a random distribution, respectively. By contrast, the distribution at (101) and (100) orientations was ~0.9-1.0 MRD and ~0.7-0.8 MRD, respectively, for both conditions. The dominance of (111) planes is rational considering these planes are of the highest coordination number of any plane and, the lowest energy for interfaces in FCC polycrystalline materials [32]. These planes are also crystallographically favourable as the $(110)_{bcc}//(111)_{fcc}$ orientation relationship during δ-ferrite to austenite phase transformation causes two growing austenite variants to intersect on (111) planes [33].

A five-parameter GBCD analysis of Σ3 and Σ9 (Fig. 4) showed a relative anisotropy in the plane distribution for both of these boundaries with a very strong peak of 45 (61) MRD at (111) planes

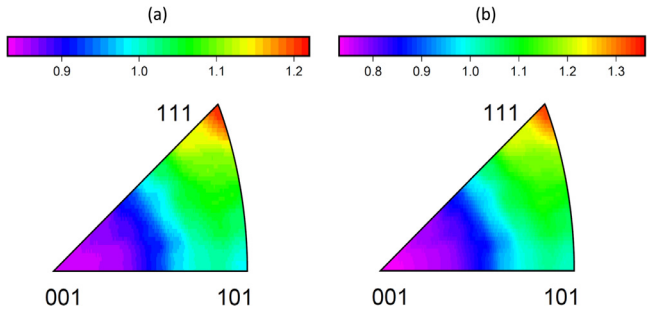

Fig. 3. Distribution of the GB planes irrespective of misorientation, expressed in the crystal lattice frames for (a) as-built and (b) annealed samples. The colour scale represents MRD.

position for Σ3 boundaries and a moderate peak of 1.1 (1.2) MRD on the zone of 90° deviation from the (110) plane for the Σ9 boundaries in the as-built (annealed) conditions. The plane distribution peak for Σ3 is of a (111)//(111) symmetric twist character representing 'coherent' twins in FCC materials [23–25]. The plane distribution peaks for the Σ9 boundaries show mostly tilt boundary characteristics with a diffuse peak on the (-221)//(-221) symmetric tilt boundary.

Generally, annealing twin formation is driven by minimisation of the total energy of the boundary network and enhancing GB mobility [34,35]. Twins can nucleate in the vicinity of sub-boundaries without requiring presence of pre-existing high-angle boundaries. Based on the preliminary model by Fullman and Fisher [34], a decrease in the free energy of the GBs is the main driving force for formation of coherent Σ3s. This has been recently confirmed by showing the minimum energy configuration occurring at the (111) plane position for Σ3 boundaries [24,36]. While coherent Σ3s are favoured by energy considerations, the formation of other Σ boundaries (e.g. Σ9) is attributed to geometrical reasons [23]. Σ9s are the consequence of two intersecting Σ3s, which do not share a common rotation axis. The character of Σ9 boundaries is thus dictated by geometrical constraints. These boundaries largely lie in the tilt region. They, however, do not always concentrate on a specific plane, as once a particular plane on one side is selected, the other one is restricted to a fixed plane dictated by the lattice misorientation [23].

Although a high frequency of boundaries in both microstructures satisfied Brandon's criterion for Σ3s, a large fraction showed a curved geometry as opposed to typical straight twin boundaries in low SFE materials. In other words, only a very small fraction of Σ3 boundaries show the parallel-sided appearance characteristic of coherent twin boundaries formed during recrystallisation. It was of interest, therefore, to elucidate the degree of coherence of these boundaries. Σ3 boundaries were classified into coherent and incoherent based on whether they are within ±10° deviation from the ideal (111) plane normal. It was found that only 36% (39%) of Σ3s were coherent in the as-built (annealed) condition. This is much lower than the volume fraction of coherent Σ3s reported in different studies on Cu [37], Ni [25], and austenite in TWIP and duplex stainless steels [24,33].

The dominance of incoherent Σ3s, which are generally of high mobility [38], implies that these boundaries sweep through the microstructure during AM. In fact, the gradients in stored energy are enough to drive boundary motion without triggering recrystallisation. This results in GBE microstructures where the intergranular pathways in the random boundary network are fragmented and replaced by mostly incoherent Σ3s. It is very interesting to see that the high mobility of incoherent Σ3 boundaries, usually adopting a curved geometry, overrides the minimum configuration energy resulting from pure twist (111) coherent boundaries during LPBF. This is consistent with the formation mechanism of curved incoherent Σ3 boundaries suggested by Randle [38]. The driving force for the GB migration correlates with its curvature; smaller radii of curvature equates to higher driving forces. Recently, it has been shown via a 3D EBSD analysis that Σ3s terminating on (111) planes on

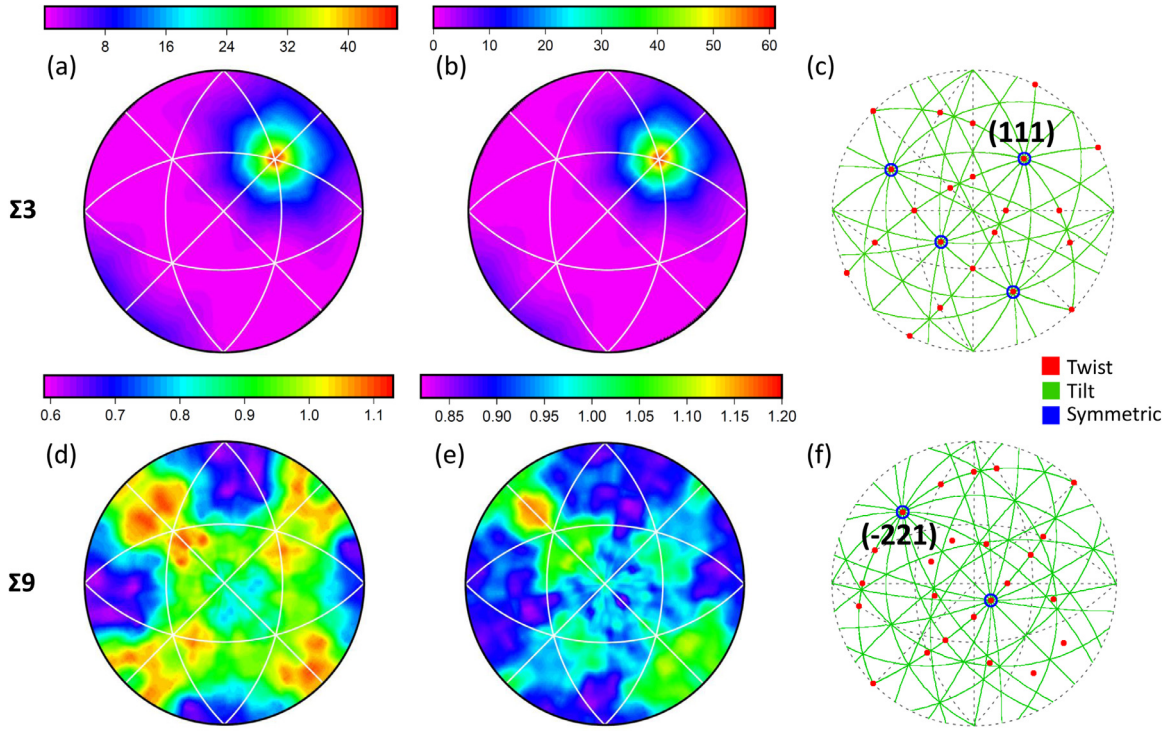

Fig. 4. Austenite-austenite GB character distribution in the (a,d) as-built and (b,e) annealed microstructures at fixed misorientations of (a,b) 60°/[111] and (d,e) 38.9°/[110]. The geometrically characteristic boundaries corresponding to each misorientation is plotted for reference in (c) and (f).

both sides are flat and show minimum curvature [39]. The maximum curvature for Σ3s was observed for boundaries that are 90° from the (111) twin position, consistent with the general assumption that twin boundaries consist of large parallel (111) coherent faces connected by perpendicular (step-like) incoherent boundaries [39].

The similarity of the GB network in the as-built and annealed conditions show that GBE occurs in-situ during AM. The first reason why LPBF samples go through incoherent Σ3 boundaries migration (kinetics effect overriding energy considerations) is because of the too low strain accumulated during LPBF for triggering DRX. The second reason may be the relatively high concentration of solute atoms in the LPBF microstructure [4,40] that not only restricts DRX, but also plays a significant role in the dominance of incoherent Σ3s. Solutes increase the activation energy for migration of random boundaries while the migration of CSL boundaries is independent of the solute content [41]. These results clearly highlight the potential for GBE during AM, though further studies on how the GB network can be changed in a targeted way via tuning the LPBF parameters are required.

In summary, a GBE-like microstructure was achieved in-situ via LPBF in a 316L SS. The evolution of microstructure was mostly dominated by kinetics i.e., the high mobility of incoherent Σ3 boundaries resulting from the strain and heat induced by thermal cycling. The GB network also consisted of random high angle, coherent Σ3 and Σ9 boundaries. Coherent Σ3s terminated on (111) pure twist boundaries due to energy and crystallography considerations while Σ9 boundaries of a tilt character were enforced by geometrical constraints. These findings provide a path for engineering the GB network of materials *in-situ* during AM.

Deakin University's Advanced Characterisation Facility is acknowledged for use of the microscopy instruments. The work at UNSW Sydney was supported by the Department of Industry, Innovation and Science, Australia (AUSMURI program). A/Prof Sophie Primig is supported under the Australian Research Council's DECRA (DE180100440) and the UNSW Scientia Fellowship schemes.

Declaration of Competing Interest

The authors declare that they have no known competing financial interests or personal relationships that could have appeared to influence the work reported in this paper.

Supplementary materials

Supplementary material associated with this article can be found, in the online version, at doi:10.1016/j.scriptamat.2020.10.018.

References

[1] I. Gibson, D.W. Rosen, B. Stucker, Additive manufacturing technologies, Springer, 2014.
[2] W.E. Frazier, J. Mater. Eng. Perform 23 (6) (2014) 1917–1928.
[3] M. Das, V.K. Balla, D. Basu, S. Bose, A. Bandyopadhyay, Scripta Mater 63 (4) (2010) 438–441.
[4] Y.M. Wang, T. Voisin, J.T. McKeown, J. Ye, N.P. Calta, Z. Li, Z. Zeng, Y. Zhang, W. Chen, T.T. Roehling, Nature materials 17 (1) (2018) 63–71.
[5] Z. Sun, X. Tan, S.B. Tor, C.K. Chua, NPG Asia Materials 10 (4) (2018) 127–136.
[6] M. Laleh, A.E. Hughes, S. Yang, J. Li, W. Xu, I. Gibson, M.Y. Tan, Corros. Sci 165 (2020) 108394.
[7] Q. Chao, V. Cruz, S. Thomas, N. Birbilis, P. Collins, A. Taylor, P.D. Hodgson, D. Fabijanic, Scripta Mater 141 (2017) 94–98.
[8] M. Laleh, A.E. Hughes, W. Xu, N. Haghdadi, K. Wang, P. Cizek, I. Gibson, M.Y. Tan, Corros. Sci 161 (2019) 108189.
[9] N. Haghdadi, M. Laleh, M. Moyle, S. Primig, Journal of Materials Science (2020), doi:10.1007/s10853-020-05109-0.
[10] C.A. Schuh, M. Kumar, W.E. King, Acta Mater 51 (3) (2003) 687–700.
[11] T. Watanabe, Journal of materials science 46 (12) (2011) 4095–4115.
[12] S. Bechtle, M. Kumar, B.P. Somerday, M.E. Launey, R.O. Ritchie, Acta Mater 57 (14) (2009) 4148–4157.
[13] V. Randle, Acta Mater 52 (14) (2004) 4067–4081.
[14] M. Shimada, H. Kokawa, Z. Wang, Y. Sato, I. Karibe, Acta Mater 50 (9) (2002) 2331–2341.
[15] T. Niendorf, S. Leuders, A. Riemer, H.A. Richard, T. Tröster, D. Schwarze, Metallurgical and Materials Transactions B 44 (4) (2013) 794–796.
[16] O. Zinovieva, A. Zinoviev, V. Romanova, R. Balokhonov, Additive Manufacturing (2020) 101521.
[17] C. Qiu, M. Al Kindi, A.S. Aladawi, I. Al Hatmi, Sci. Rep 8 (1) (2018) 1–16.
[18] G.S. Rohrer, D.M. Saylor, B.E. Dasher, B.L. Adams, A.D. Rollett, P. Wynblatt, Z. Metallk 95 (4) (2004) 197–214.
[19] A. Morawiec, J. Appl. Crystallogr 44 (6) (2011) 1152–1156.
[20] S.-H. Sun, T. Ishimoto, K. Hagihara, Y. Tsutsumi, T. Hanawa, T. Nakano, Scripta Mater 159 (2019) 89–93.
[21] D. Brandon, Acta Metall 14 (11) (1966) 1479–1484.
[22] S. Xia, B. Zhou, W. Chen, Metallurgical and materials transactions A 40 (12) (2009) 3016.
[23] G.S. Rohrer, V. Randle, C.-S. Kim, Y. Hu, Acta Mater 54 (17) (2006) 4489–4502.
[24] H. Beladi, N.T. Nuhfer, G.S. Rohrer, Acta Mater 70 (2014) 281–289.
[25] J. Li, S.J. Dillon, G.S. Rohrer, Acta Mater 57 (14) (2009) 4304–4311.
[26] M. Kumar, A.J. Schwartz, W.E. King, Acta Mater 50 (10) (2002) 2599–2612.
[27] J.B. Koo, D.Y. Yoon, M.F. Henry, Metallurgical and materials transactions A 33 (12) (2002) 3803–3815.
[28] R.E. García, M.D. Vaudin, Acta Mater 55 (17) (2007) 5728–5735.
[29] K. Kurzydłowski, B. Ralph, J. Bucki, A. Garbacz, Materials Science and Engineering: A 205 (1-2) (1996) 127–132.
[30] M. Shamsujjoha, S.R. Agnew, J.M. Fitz-Gerald, W.R. Moore, T.A. Newman, Metallurgical and Materials Transactions A 49 (7) (2018) 3011–3027.
[31] T. Watanabe, Materials Science and Engineering: A 176 (1-2) (1994) 39–49.
[32] J. Mackenzie, A. Moore, J. Nicholas, J. Phys. Chem. Solids 23 (3) (1962) 185–196.
[33] N. Haghdadi, P. Cizek, P. Hodgson, V. Tari, G. Rohrer, H. Beladi, Acta Mater 145 (2018) 196–209.
[34] R. Fullman, J. Fisher, J. Appl. Phys 22 (11) (1951) 1350–1355.
[35] G. Gindraux, J. INST. METALS 101 (1973) 85–93.
[36] B. Lin, Y. Jin, C.M. Hefferan, S.F. Li, J. Lind, R.M. Suter, M. Bernacki, N. Bozzolo, A.D. Rollett, G.S. Rohrer, Acta Mater 99 (2015) 63–68.
[37] A. Darbal, K. Ganesh, X. Liu, S. Lee, J. Ledonne, T. Sun, B. Yao, A. Warren, G. Rohrer, A. Rollett, Microsc. Microanal 19 (1) (2013) 111.
[38] V. Randle, Acta Mater 47 (15-16) (1999) 4187–4196.
[39] X. Zhong, D.J. Rowenhorst, H. Beladi, G.S. Rohrer, Acta Mater 123 (2017) 136–145.
[40] Y. Zhong, L. Liu, S. Wikman, D. Cui, Z. Shen, J. Nucl. Mater 470 (2016) 170–178.
[41] G. Palumbo, K. Aust, Can. Metall. Q 34 (3) (1995) 165–173.